Bessel-Gauss Beams Through Leaky Waves: Focusing and Diffractive Properties

Walter Fuscaldo[1,*] Alessio Benedetti,[1] Davide Comite,[1] Paolo Baccarelli,[2] Paolo Burghignoli,[1] and Alessandro Galli[1]

[1]*Department of Information Engineering, Electronics and Telecommunications, Sapienza University of Rome, Via Eudossiana 18, Rome 00184, Italy*
[2]*Department of Engineering, Roma Tre University, Via Vito Volterra 62, Rome 00146, Italy*

Bessel-Gauss beams have mainly been proposed in optics as a solution for reducing the on-axis intensity oscillations typical of Bessel beams. Previous investigations on Bessel-Gauss beams are based on a scalar theory in the paraxial approximation, and thus cannot be extended to the microwave range where a fully vectorial approach is needed. Here, the generation of Bessel-Gauss beams through leaky waves is investigated. First, the nondiffractive and focusing properties of Bessel-Gauss beams generated through leaky waves are extensively examined in the frame of a vectorial approach. Useful design criteria are derived to optimize both the radiation and the focusing efficiency of such beams. On this basis, leaky-wave radiators synthesized to support the generation of a Bessel-Gauss beam over a given frequency band in the microwave range are presented. Full-wave results corroborate the concept.

I. INTRODUCTION

Bessel beams (BBs) are ideal solutions of the Helmholtz equation in a cylindrical reference frame [1]. However, they became widespread in optics only in the early 1990s when their practical generation from finite apertures was demonstrated (see, e.g., Refs. [2–4]).

Bessel beams are, in principle, *diffraction-free* beams [3], and this property makes them particularly appealing in a plethora of modern applications spanning the frequency range from microwaves to optics, and even beyond. In addition to the nondiffractive properties, BBs also retain a remarkable *focusing* and *self-healing* character (i.e., the capability to reconstruct themselves if an obstacle is put across the propagation axis) [5].

As opposed to diffractive beams, such as *Gaussian beams* (GBs), the amount of energy carried within the main lobe of a BB is just a small fraction of the total energy. Nevertheless, this limitation does not considerably hinder the efficiency of BBs in focusing applications, as demonstrated in Ref. [4]. Indeed, the more efficient initial energy distribution of GBs (that, conversely, carry most of their energy within the main lobe) is partially washed out after the Rayleigh distance, because of diffractive spreading. In fact, comparison between the propagation properties of GBs and BBs with equal initial beam waist set to a fraction $1/N$ of the radiating aperture reveals that BBs would cover N times the distance covered by a GB at the expense of a $1/N$ power efficiency [4].

It would be interesting however to ascertain the benefits of combining the properties of GBs with those of BBs, and to determine to what extent this combination would affect their propagation properties. In this regard, it is worth noting that *Bessel-Gauss* beams (BGBs) have already been proposed in optics to reduce the on-axis oscillations of the intensity of BBs, notably due to diffraction contributions from edges [6–11].

On the other hand, the current literature still lacks a thorough investigation of the nondiffractive properties of BGBs, as well as a detailed analysis on the effects related to the choice of the Gaussian beam waist parameter. Indeed, most of the works discussing the propagation characteristics of BGBs and BBs (see, e.g., Refs. [12–22]) are mainly focused on the effects of the *apodization* on the on-axis distribution, rather than the focusing character over the transverse plane, and are limited to a few case studies. Moreover, results in Refs. [19–21,23] are derived under the frame of a *scalar theory* and the *paraxial approximation*. The first hypothesis limits the analysis to few polarization states, whereas it has been proven that both Bessel [24,25] and Bessel-Gauss [8] beams with arbitrary polarizations can be derived as solutions of the *vector* Helmholtz equation. The second hypothesis limits the analysis to beams with waists that are large with respect to the operating wavelength, and are thus of limited interest in the microwave range [26,27]. Efforts to include higher-order *nonparaxial* corrections to the paraxial BGB

---

*wal.fuscaldo@gmail.com

solution in analytical closed form have been discussed in Ref. [22]. However, results were derived in the infinite aperture case, thus limiting the analysis to beam waists that are considerably smaller than the aperture diameter.

In this work, we aim to analyze the nondiffractive and focusing properties of *nonparaxial* BGBs of *any* beam-waist size under the frame of a vectorial approach, in order to apply these results to the generation of BGBs at microwave frequencies. In this regard, we should stress that BGBs have few experimental validations in the microwave range. On the other hand, BBs can be generated through various techniques (see, e.g., Refs. [26–34]). Here, we focus only on those systems based on *leaky waves* [35,36]. In this regard, we should mention that *leaky-wave* Bessel beams (LW BBs) possess slightly different non-diffractive properties with respect to *classical* BBs owing to the intrinsic exponentially decaying character of the aperture distribution [36]. Nevertheless, leaky-wave theory offers a rigorous, straightforward, and flexible method to modulate the aperture distribution in order to synthesize a target amplitude profile [37–40]. In this specific case, we address the synthesis procedure of a BGB through leaky waves.

The outline of this paper is as follows. In Sec. II, moving from the ray-optics explanation of *classical* BBs [41,42], we extend the analysis to LW BBs and BGBs. Comparison of these results offers a first qualitative overview of the propagation properties of such beams. In Sec. III, we provide an extensive, fully vectorial numerical analysis of the nondiffractive and focusing properties of BGBs for several different choices of the relevant design parameters, namely the axicon angle and the Gaussian beam waist. The flux of the radial and longitudinal components of the Poynting vector is also evaluated to determine the power-transport properties of BGBs. In Sec. IV, the synthesis procedure needed for the generation of BGBs through leaky waves is outlined. Numerical full-wave results are shown for two leaky-wave structures designed according to the criteria described in the previous two sections. A conclusive discussion is provided in Sec. V.

II. BESSEL BEAMS, LEAKY-WAVE BESSEL BEAMS, BESSEL-GAUSS BEAMS

We here review, under the frame of a scalar theory and the ray-optics approximation, some basic properties of *classical* BBs, i.e., beams whose aperture field distribution is described by a cylindrical function of a *real* argument, and LW BBs, i.e., BBs generated through *leaky waves*, and thus described by a cylindrical function of a *complex* argument [36]. This allows us to easily derive the propagation properties of BGBs and compare them with those of BBs and LW BBs. In the scalar approximation, the propagation features of Bessel beams can qualitatively be predicted under a ray-optics interpretation.

Let us consider a radiating aperture of radius ρ_{ap} supporting an inward cylindrical aperture distribution $A(\rho)$ of the type

$$A(\rho) \propto H_0^{(1)}(k_\rho \rho) \sim \frac{e^{jk_\rho \rho}}{\sqrt{\rho}}, \quad (1)$$

where $H_n^{(1)}$ represents the *n*th-order Hankel function of the first kind (an $e^{j\omega t}$ time dependence is assumed and suppressed throughout this paper), and $k_\rho = k_0 \sin \theta_0$ with $k_\rho \in \mathbb{R}^+$ the *real positive* radial wave number, k_0 the free-space wave number, and θ_0 the axicon angle, measured from the vertical z axis. (The asymptotic relation (1) holds for large arguments.) It is well known [41,42] that the aperture distribution in Eq. (1) is capable of producing a Bessel beam in the near-field region. Indeed, a plane-wave spectral representation of such an aperture field shows that it can be interpreted as a superposition of plane waves whose wavevectors lie in the close vicinity of the surface of a cone with axis parallel to the z axis and aperture $2\theta_0$; under the ray-optics approximation, such plane waves can be associated with rays emitted from the aperture at an angle $\theta_0 = \arcsin(k_\rho/k_0) \in [0, \pi/2]$ [43], as shown in Fig. 1(a). As extensively discussed in Refs. [41,42], for such an aperture distribution, a Bessel beam is created over a diamond-shaped region, whose vertex defines the so-called nondiffractive range $z_{ndr} = \rho_{ap} \cot \theta_0$. For $z < z_{ndr}$, the on-axis (i.e., $\rho = 0$) field amplitude $E(0,z)$ is constant (neglecting the typical oscillations due to diffraction contributions from the edge), while for $z > z_{ndr}$ it rapidly decays. (We note that, under the ray-optics approximation, the on-axis field amplitude halves at $z = z_{ndr}$.) The interested reader can find more accurate analytical descriptions in Ref. [44].

When dealing with *leaky-wave* aperture fields, one should account for the *complex* nature of the radial wave number $k_\rho = \beta_\rho - j\alpha_\rho$, where β_ρ and α_ρ are the phase and attenuation (or leakage) constants, respectively. For such complex waves, we now have $\theta_0 = \arcsin(|\beta_\rho|/k_0)$, where the real positive part of k_ρ is taken to ensure $\theta_0 \in [0, \pi/2]$ in the case of *complex rays* characterized by complex wave numbers [43].

It is worth recalling here that a simple source, such as a vertical electric dipole (VED), in a partially open two-dimensional (2D) uniform planar waveguide made of ordinary materials can excite a *forward*, fast (i.e., $0 < \beta_\rho < k_0$) cylindrical leaky wave [45,46], thus giving rise to an outward cylindrical aperture distribution (which cannot focus radiation around the axis of symmetry), instead of the required inward cylindrical aperture distribution. However, if a radially periodic grating is placed on top of the structure, the period can be selected in order to have the $n = -1$ Floquet harmonic (note that the radially periodic nature of the grating allows for describing the electromagnetic field in terms of a complete infinite set of Floquet

(a)

Outward rays $H_0^{(2)}(k_\rho\rho)$ Inward rays $H_0^{(1)}(k_\rho\rho)$ Diamond region of constructive interference

$z_{\mathrm{ndr}} = \rho_{\mathrm{ap}}\cot\theta_0$

$\theta_0 = \arcsin\left(\dfrac{k_\rho}{k_0}\right)$

Nondiffractive range

$\rho = \rho_{\mathrm{ap}}$

Inward cylindrical aperture distribution

$H_0^{(1)}(k_\rho\rho),\ k_\rho \in \mathbb{R}^+$ No amplitude variation

(b)

Intensity decay due to aperture amplitude modulation

$z_{\mathrm{ndr}} = \rho_{\mathrm{ap}}\cot\theta_0$

$z_{\mathrm{ndr}}^{\mathrm{BG}} = z_{\mathrm{ndr}}\,\tilde{w}_0\sqrt{\ln 4}$

Nondiffractive range

Grating

$\rho = \rho_{\mathrm{ap}}$

Ground plane   Source

Backward wave $\begin{cases} k_\rho = \beta_\rho - j\alpha_\rho \in \mathbb{C} \\ \beta_\rho < 0,\ \alpha_\rho > 0 \end{cases}$

$H_0^{(2)}\!\left[\left(\beta_\rho - ja_\rho\right)\rho\right] = -H_0^{(1)}\!\left[-\left(\beta_\rho - ja_\rho\right)\rho\right]$

$\Downarrow$

$H_0^{(2)}\!\left[\left(\beta_\rho - j\alpha_\rho\right)\rho\right] \sim C\,\dfrac{e^{-j\beta_\rho\rho}}{\sqrt{\rho}}e^{-\alpha_\rho\rho}$ Leaky-wave amplitude variation

$H_0^{(2)}(\beta_\rho\rho)e^{-\frac{1}{2}\left(\frac{\rho}{w_0}\right)^2} \sim C'\,\dfrac{e^{-j\beta_\rho\rho}}{\sqrt{\rho}}e^{-\frac{1}{2}\left(\frac{\rho}{w_0}\right)^2}$ Gaussian amplitude variation
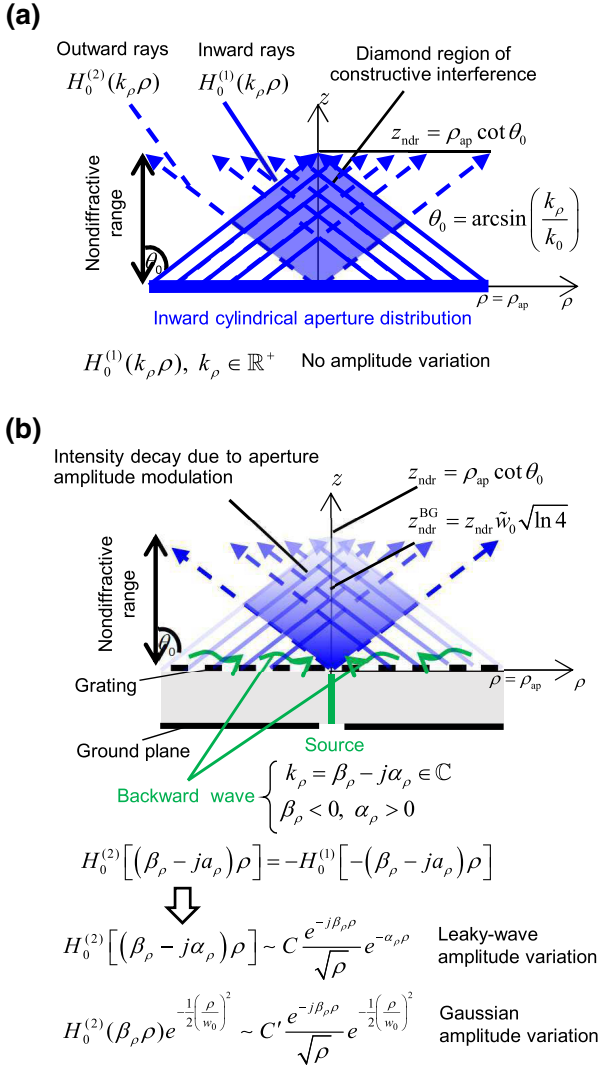
FIG. 1. Ray-optics interpretation of (a) *classical* Bessel beams and (b) either *leaky-wave* Bessel beams (LW-BBs) or Bessel-Gauss beams (BGBs). In (a) classical BBs are generated assuming a *constant-amplitude* inward aperture distribution; each ray equally contributes to the field over a diamond-shaped region where inward and outward rays constructively interfere to produce a BB pattern. In (b) LW BBs or BGBs are generated assuming a *radially varying* inward aperture distribution; each ray contributes with a different weight to the field, and the color gradient in the diamond-shaped region represents the progressive decay of the field amplitude. The inward aperture distribution is recovered from the backward wave (solid green wavy arrows) supported by the radially periodic grating. Note that LW BBs (BGBs) asymptotically differ from *classical* BBs for an exponentially decaying (Gaussian) amplitude factor.

the first and second kind [[47], Eq. (9.1.39)]. Because of the complex nature of the leaky wave number, when leaky radial waveguides as those in Refs. [26,33,35,36] are used for generating Bessel beams, the aperture field distribution should account for an additional exponentially decaying amplitude factor of the kind $e^{-\alpha_\rho\rho}$ [see Fig. 1(b)]. Therefore, a LW BB is described by the aperture distribution

$$A(\rho) \propto H_0^{(2)}(k_\rho\rho) \sim \frac{e^{-j\beta_\rho\rho}}{\sqrt{\rho}}e^{-\alpha_\rho\rho} \quad \text{for } \beta_\rho < 0, \alpha_\rho > 0, \tag{2}$$

where $H_n^{(2)}$ represent the nth-order Hankel function of the second kind. The asymptotic relation explicitly reveals the effect of the complex *leaky* nature of the radial wave number on the aperture distribution with respect to Eq. (1).

The amplitude variation of the aperture distribution unavoidably affects the on-axis field amplitude distribution that, for $z < z_{\mathrm{ndr}}$, is no longer constant, but takes the expression [36]

$$\frac{|E(0,z)|}{|E(0,0)|} = e^{-\alpha_\rho z \tan\theta_0}, \qquad z < z_{\mathrm{ndr}}, \tag{3}$$

where $|E(0,z)|$ has been conveniently normalized to its initial value $|E(0,0)|$. If we define the nondiffractive range for LW BBs $z_{\mathrm{ndr}}^{\mathrm{LW}}$ as $|E(z_{\mathrm{ndr}}^{\mathrm{LW}},0)| = |E(0,0)|/2$, the following expression is easily found:

$$z_{\mathrm{ndr}}^{\mathrm{LW}} = \begin{cases} z_{\mathrm{ndr}}\dfrac{\ln\sqrt{2}}{\pi\hat{\alpha}_\rho\bar{\rho}_{\mathrm{ap}}}, & \dfrac{\ln\sqrt{2}}{\pi\bar{\rho}_{\mathrm{ap}}} < \hat{\alpha}_\rho \ll 1, \\[4mm] z_{\mathrm{ndr}}, & \hat{\alpha}_\rho \leq \dfrac{\ln\sqrt{2}}{\pi\bar{\rho}_{\mathrm{ap}}} \ll 1. \end{cases} \tag{4}$$

Here a hat and a bar denote normalization with respect to $k_0 = 2\pi/\lambda_0$ and λ_0, respectively. It is worth commenting on the range of validity of this expression. The upper bound $\hat{\alpha}_\rho \ll 1$ is dictated by the condition for having a physically significant leaky wave [48,49], whereas the lower bound $\hat{\alpha}_\rho > \ln\sqrt{2}/(\pi\bar{\rho}_{\mathrm{ap}})$ is required to avoid cases for which $z_{\mathrm{ndr}}^{\mathrm{LW}} > z_{\mathrm{ndr}}$ that would arise from Eq. (4) because Eq. (3) neglects the aperture truncation.

It is interesting to relate $\hat{\alpha}_\rho$ to the leaky-wave radiation efficiency η through the relation $\eta = 1 - \exp(-4\pi\hat{\alpha}_\rho\bar{\rho}_{\mathrm{ap}})$ [37]. Indeed, after simple algebraic steps, it is possible to show that Eq. (4) is equivalent to

$$z_{\mathrm{ndr}}^{\mathrm{LW}} = z_{\mathrm{ndr}}\frac{\ln 4}{\ln[1/(1-\eta)]}, \qquad 0.75 < \eta < 1. \tag{5}$$

Since leaky-wave radiators are commonly sized to have $\eta \simeq 0.9$, the lower bound is not a restrictive condition.

The same approach can be exploited to derive an approximate analytic expression for the nondiffractive

harmonics) radiating with a specific angle at a given frequency. As a result, a *backward*, fast (i.e., $-k_0 < \beta_\rho < 0$) cylindrical leaky wave would be excited, giving rise to the required inward cylindrical aperture distribution [exploiting the well-known relation between Hankel functions of

range of a BGB, which can be described by the aperture distribution [cf. Fig. 1(b)]

$$A(\rho) \propto H_0^{(2)}(\beta_\rho \rho) e^{-(1/2)(\rho/w_0)^2} \sim \frac{e^{-j\beta_\rho}}{\sqrt{\rho}} e^{-(1/2)(\rho/w_0)^2},$$
(6)

where $\beta_\rho < 0$ and w_0 is the Gaussian beam waist parameter. Indeed, by replacing the exponentially decaying variation of LW BBs [see Eq. (2)] with the Gaussian modulation of BGBs [see Eq. (6)], the on-axis field amplitude distribution reads

$$\frac{|E(0,z)|}{|E(0,0)|} = e^{-(1/2)[(z/w_0)\tan\theta_0]^2}, \qquad z < z_{\text{ndr}}.$$
(7)

As for LW BBs, a nondiffractive range for BGBs $z_{\text{ndr}}^{\text{BG}}$ such that $|E(z_{\text{ndr}}^{\text{BG}}, 0)| = |E(0,0)|/2$ is easily found from Eq. (7), i.e.,

$$z_{\text{ndr}}^{\text{BG}} = \begin{cases} z_{\text{ndr}}\tilde{w}_0\sqrt{\ln 4}, & \tilde{w}_0 < \dfrac{1}{\sqrt{\ln 4}}, \\[2mm] z_{\text{ndr}}, & \tilde{w}_0 \geq \dfrac{1}{\sqrt{\ln 4}}, \end{cases}$$
(8)

where a tilde denotes normalization with respect to ρ_{ap}, and the upper bound for $\tilde{w}_0 \equiv w_0/\rho_{\text{ap}}$ is again needed to avoid cases for which $z_{\text{ndr}}^{\text{BG}} > z_{\text{ndr}}$. We should stress that, under the ray-optics approximation, Eq. (8) extends the classical nondiffractive range formula that holds only for BBs [2] to the more general case of BGBs. In the asymptotic limit $\tilde{w}_0 \to 0$ and $\tilde{w}_0 \to \infty$, a BGB converges to a GB and a BB, respectively; this aspect is correctly recovered by Eq. (8) for which we have $\lim_{\tilde{w}_0 \to 0} z_{\text{ndr}}^{\text{BG}} = 0$ (in agreement with the *diffractive* nature of GBs) and $\lim_{\tilde{w}_0 \to \infty} z_{\text{ndr}}^{\text{BG}} = z_{\text{ndr}}$. More precisely, Eq. (8) predicts that $z_{\text{ndr}}^{\text{BG}} = z_{\text{ndr}}$ for $\tilde{w}_0 > \tilde{w}_{0,\text{lim}}$, where $\tilde{w}_{0,\text{lim}} = 1/\sqrt{\ln 4} \simeq 0.85$. It is worth commenting here that GBs are more commonly obtained from BGBs under the asymptotic condition $\theta_0 \to 0°$. This is however the paraxial-limit hypothesis for which results have already been reported in Refs. [19–21,23] and are thus not discussed here. Nevertheless, we should comment that, in the *nonparaxial limit*, a BGB approaches a GB anytime $\tilde{w}_0$ is smaller than the normalized BB waist. If we measure the BB waist as the null-to-null distance of the zeroth-order Bessel function of the first kind (we define $j_{0,1} \simeq 2.405$ the first null of J_0) then $\tilde{w}_0 < j_{0,1}/(2\pi \sin\theta_0 \bar{\rho}_{\text{ap}})$ [[50], Eq. (5)] sets a condition for having a BGB approaching a GB in the nonparaxial limit.

In addition, comparison between Eqs. (5) and (8) yields the condition for having a BGB with a nondiffractive range

greater than a LW BB in terms of η and $\tilde{w}_0$:

$$\frac{\ln 4}{\ln[1/(1-\eta)]} < \frac{\tilde{w}_0}{\tilde{w}_{0,\text{lim}}} < 1, \qquad 0.75 < \eta < 1.$$
(9)

We note that the condition $0.75 < \eta < 1$ ensures the consistency of Eq. (9): within this range of η the lower bound of Eq. (9) is always lower than its upper bound. From Eq. (9), and neglecting cases for which $\eta < 0.9$, we find that significant values of $\tilde{w}_0$ should range from 0.5 to 0.85. This interval may be interpreted as follows: a BGB with $\tilde{w}_0 > 0.85$ covers the nondiffractive distance of a *pure* BB, whereas a BGB with $\tilde{w}_0 < 0.5$ covers the same nondiffractive distance of a LW BB with $\eta = 0.9$. This result constitutes a preliminary guideline for the synthesis of Bessel-Gauss beam launchers based on leaky waves.

The results obtained in this section under the frame of a scalar theory will be compared with fully-vectorial numerical results in Sec. III, where the effects of the normalized beam waist parameter $\tilde{w}_0$ and the axicon angle θ_0 (beyond the paraxial limit) will be thoroughly investigated.

III. DIFFRACTIVE, FOCUSING, AND POWER TRANSPORT PROPERTIES OF BESSEL-GAUSS BEAMS

In this section we comment on the results obtained through accurate numerical simulations for several cases of interest. The methods used for performing the numerical simulations are described in Sec. III A, whereas in the following two sections the diffractive, focusing (Sec. III B) and power transport (Sec. III C) properties of BGBs are evaluated and compared with the theoretical predictions of Sec. II.

A. Methods

Our investigation addresses beams having TM^z polarization and no azimuthal variation (zeroth-order beams), such as those that would be excited on a planar structure by, e.g., a VED source placed along the z axis. For such beams, the only nonzero components are E_ρ, E_z, and H_ϕ. In particular, the electric field on the aperture plane $z = 0$ can be analytically expressed as

$$\begin{aligned} E_{\text{ap},z}(\rho) &= E_0 \mathcal{C}_0(k_\rho \rho), \\ E_{\text{ap},\rho}(\rho) &= j\frac{k_z}{k_\rho} E_0 \mathcal{C}_1(k_\rho \rho). \end{aligned}$$
(10)

Here $k_z = \sqrt{k_0^2 - k_\rho^2}$ (with $\text{Im}\{k_z\} < 0$) is the vertical wave number in the air region $z > 0$ and $\mathcal{C}_{0,1}(\cdot)$ indicates a cylindrical function that is a Bessel function of the first kind, $J_{0,1}(\cdot)$, for stationary aperture distributions (see, e.g., Refs. [26,27]), whereas it is the Hankel function of the first kind, $H_{0,1}^{(1)}(\cdot)$, or second kind, $H_{0,1}^{(2)}(\cdot)$, for inward

or outward aperture distributions, respectively, as those considered here [see Eqs. (1), (2), and (6)].

Near-field distributions in the half space $z > 0$ will be illustrated, considering in particular the vertical component of the electric field E_z, whose radial dependence is expressed by a cylindrical function of order 0 [cf. the first line of Eq. (10)]. Such distributions are obtained from the tangential components of the aperture electric field $\mathbf{E}_{ap}$ by using standard radiation integrals. In particular, for the electric field, we have

$$\mathbf{E}(\mathbf{r}) = -2 \int_{\Sigma_A} \mathbf{R} \times [\mathbf{E}_{ap}(\mathbf{r}') \times \mathbf{u}_z] \frac{1 + jk_0|\mathbf{R}|}{4\pi|\mathbf{R}|^3} e^{-jk_0|\mathbf{R}|} \, d\mathbf{r}',$$

$$\mathbf{H}(\mathbf{r}) = \frac{j}{k_0\eta_0} \nabla \times \mathbf{E}(\mathbf{r}),$$

$$(11)$$

with $\mathbf{R} = \mathbf{r} - \mathbf{r}'$, where $\mathbf{r}$ and $\mathbf{r}'$ are the position vectors of the observation and source points, respectively, $\eta_0 \simeq 377\ \Omega$ is the free-space impedance, $\mathbf{u}_z$ is the unit vector of the z axis, and the integration domain is the aperture plane Σ_A. Such radiation integrals have been evaluated numerically, by properly managing the singularities of the integrand that typically arise from their kernel (i.e., the free-space Green's function) for observation points at or close to the plane $z = 0$. Furthermore, for LW BBs, an integrable singularity also occurs on the axis $\rho' = 0$ for any observation point, owing to the singularity at the origin of the Hankel functions of the first and second kind, $H_1^{(1)}(k_\rho\rho')$ and $H_1^{(2)}(k_\rho\rho')$, which expresses the radial dependence of the relevant tangential fields [cf. the second line of Eq. (10)].

The power-transport properties of the considered beams will also be illustrated, considering the average flux of power across the surface of a finite cylinder whose axis is the z axis and whose length spans a range from 0 to the nondiffractive range and beyond. The radius of the cylinder is chosen to coincide with the first null of the Bessel function $J_0(k_\rho\rho)$, in order to ascertain the capability of the beam to focus the radiated power in the vicinity of the z axis.

B. Diffractive and focusing properties

We first validate the accuracy of Eq. (8). For this purpose, we numerically evaluate z_{ndr}^{BG} on a large dataset, namely for several values of θ_0 ranging from $10°$ to $80°$ and $\tilde{w}_0$ ranging from 0.2 and 1.6, following the procedure described in the Appendix. In Fig. 2 we show results from the numerical dataset (left-hand panel) and compare them with the analytical results (right-hand panel) obtained with Eq. (8). The nondiffractive range is evaluated as a function of θ_0 and $\tilde{w}_0$ for a fixed aperture radius $\rho_{ap} = 30\lambda_0$; however, very similar results are obtained for a different aperture radius provided that $\rho_{ap} \gg \lambda_0$. Therefore, in
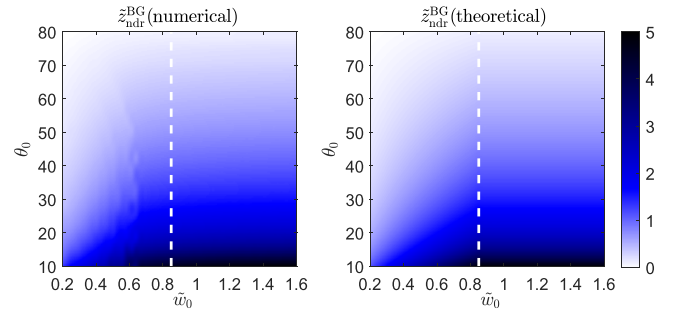

FIG. 2. The nondiffractive range normalized to the aperture radius $\tilde{z}_{ndr}^{BG}$, as a function of θ_0 and $\tilde{w}_0$, is evaluated numerically (left) and through Eq. (8) (right). A vertical dashed white line highlights the limiting value $\tilde{w}_0 = \tilde{w}_{0,lim}$.

Fig. 2 we show the nondiffractive range normalized to the aperture radius and defined as $\tilde{z}_{ndr}^{BG} = z_{ndr}^{BG}/\rho_{ap}$. Very good agreement is observed between the numerical results and the theoretical predictions. We also note that the numerical evaluation for $\tilde{w}_0 \simeq \tilde{w}_{0,lim}$ is slightly lower than the asymptotic value predicted by Eq. (8), viz., z_{ndr}; however, the numerical estimation converges to z_{ndr} at $\tilde{w}_0 \simeq \tilde{w}_{0,lim}$ as $\rho_{ap}/\lambda_0 \to \infty$, in agreement with the ray-optics approximation. In this asymptotic condition the BGB solution converges to the BB solution. It is also worth noting that, for $\theta_0 \to 0°$ (i.e., approaching the paraxial limit) and $\tilde{w}_0 > \tilde{w}_{0,lim}$, $z_{ndr} \to \infty$, i.e., the BGB solution converges to the plane-wave solution [23], whereas for $\theta_0 \to 0°$ and $\tilde{w}_0 < \tilde{w}_{0,lim}$, the nondiffractive feature is mainly determined by $\tilde{w}_0$, and the BGB solution converges to the GB solution.

We now discuss the effect of the beam waist parameter $\tilde{w}_0$ on the focusing properties of BGBs considering an aperture radius $\rho_{ap} = 20\lambda_0$ and an axicon angle $\theta_0 = 30°$ (the effect of a different θ_0, although well known, is shown later for a few cases). In Fig. 3(a), color maps of the vertical component of the electric field E_z are shown for different values of $\tilde{w}_0$ [see Fig. 3(a) from left to right] ranging from a very high value ($\tilde{w}_0 \to \infty$) to a very low value ($\tilde{w}_0 = 0.2$). For these two limiting values of $\tilde{w}_0$, the BGB can be considered to have asymptotically converged to a BB and a GB, respectively. In all cases, the electric field amplitudes are normalized to their respective maxima attained around $\rho = 0$, $z \to 0$. As shown, by decreasing $\tilde{w}_0$, the nondiffractive range decreases, according to Eq. (8). Numerical evaluations of z_{ndr}^{BG} and Eq. (8) are highlighted with black bars and open circles, respectively (a more complete validation is shown next).

In Fig. 3(b), the radial cuts of the BGB at $z_0 = z_{ndr}^{BG}/2$ (solid blue lines) and $z_0 = z_{ndr}^{BG}$ (solid light blue lines) are compared with the theoretical distributions expected for an *ideal* BB [i.e., given by $J_0(k_\rho\rho)$] and an *ideal* BGB [i.e., given by $J_0(k_\rho\rho)e^{-\rho^2/(2w_0^2)}$] generated with the same parameters (i.e., same θ_0 and $\tilde{w}_0 \to \infty$, and same θ_0 and $\tilde{w}_0$, respectively). It is seen that, as $\tilde{w}_0$ decreases, the
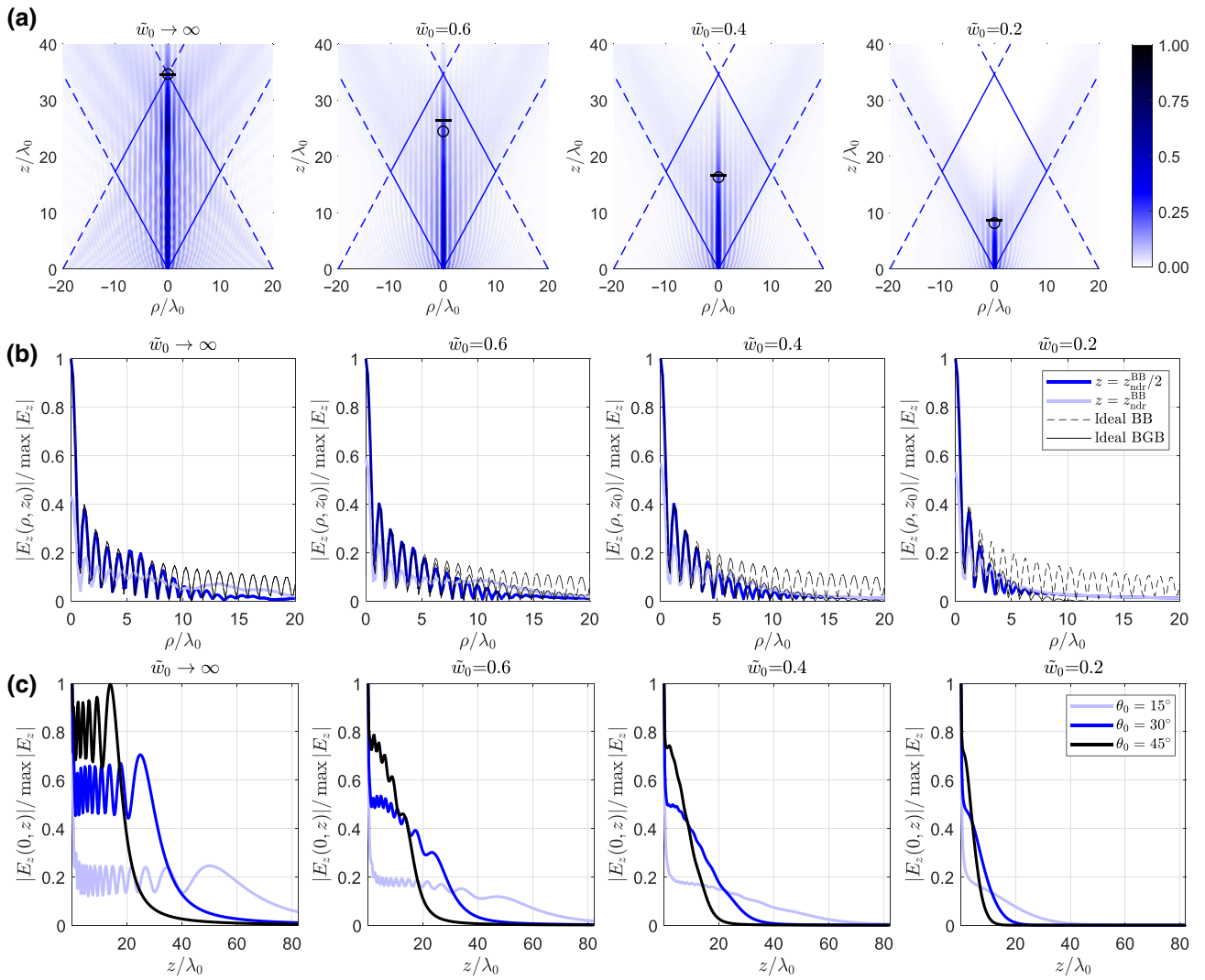
FIG. 3.   (a) Color maps of the absolute value of the E_z component of the electric field over the x-z plane in the range $|\rho| < \rho_{\mathrm{ap}} = 20\lambda_0$ and $0 < z < 40\lambda_0$. From left to right, $\tilde{w}_0$ decreases from a very large value (close to the asymptotic condition for having a BB, i.e., $\tilde{w}_0 \to \infty$) up to $\tilde{w}_0 = 0.2$ (close to the asymptotic condition for having a GB, i.e., $\tilde{w}_0 \to 0$). The black bars and open circles represent the numerical calculations and analytical estimations through Eq. (8) of $z_{\mathrm{ndr}}^{\mathrm{BB}}$, respectively. (b) Radial 1D electric field profiles at $z_0 = z_{\mathrm{ndr}}^{\mathrm{BB}}/2$ (blue solid lines) and $z_0 = z_{\mathrm{ndr}}^{\mathrm{BB}}$ (light blue solid lines) for different values of $\tilde{w}_0$ from left to right [the same as in (a)]. The electric field profiles are normalized to their respective maxima for each different value of $\tilde{w}_0$, and compared with the theoretical profiles of an ideal BB (black dashed line) and an ideal BGB (black solid line). (c) On-axis 1D electric field profiles for different $\tilde{w}_0$ from left to right [the same as in (a)], and different axicon angles $\theta_0 = 15°$, $\theta_0 = 30°$, $\theta_0 = 45°$, in light blue, blue, and black continuous lines, respectively.

intensity of the sidelobes decreases, thus improving the focusing properties at the expense of a reduced nondiffractive range.

In Fig. 3(c), the effects of both $\tilde{w}_0$ and θ_0 on the on-axis profiles are shown. As already commented in Ref. [7], a lower value of $\tilde{w}_0$ reduces the on-axis oscillations, but also reduces the nondiffractive range. Conversely, a lower value of θ_0 increases the nondiffractive range, but unavoidably lowers the average field intensity owing to energy conservation. It can be inferred from Fig. 3 that the product between the average field intensity and the corresponding

nondiffractive range is independent of both θ_0 and $\tilde{w}_0$ [e.g., from Fig. 3(c), the ratio between the average field intensity of the E_z profiles for $\theta_0 = 45°$ and $\theta_0 = 15°$ is about 4, and the ratio between the corresponding nondiffractive ranges is about 1/4, for any choice of $\tilde{w}_0$].

C. Power-transport properties

From Sec. III B, it has emerged that BGBs furnish an additional degree of freedom with respect to either BBs ($\tilde{w}_0$ in addition to θ_0) or GBs (θ_0 in addition to $\tilde{w}_0$) to profitably

adjust the focusing and nondiffractive properties of the beam according to the requirements of a considered application. Nonetheless, it is also important to investigate how the power-transport properties are affected by changing the beam waist parameter $\tilde{w}_0$ for a given θ_0.

A similar analysis was proposed in Ref. [4] to compare the power transport properties of BBs and GBs under the paraxial approximation, thus ignoring the vectorial nature of electromagnetic fields. That work revealed that BBs and GBs generated by radiating apertures of the same size exhibit comparable *power-transport efficiency*, defined as the ratio between the power flux over a given area at a certain distance and the total initial power (i.e., the power flux over the entire radiating aperture). Here, we thoroughly evaluate the power transport efficiency of BGBs at different distances z_0 from the radiating aperture and for different $\tilde{w}_0$, accounting for the vectorial nature of the electromagnetic field.

As discussed in Sec. III A, a TM^z-polarized zeroth-order BB possesses nonzero E_ρ, E_z, and H_ϕ components; thus, the Poynting vector $\mathbf{S} = (1/2)\mathbf{E} \times \mathbf{H}^*$ will have both S_ρ and S_z nonzero components. With reference to the geometry schematized in Fig. 4, the average power transported by a BGB at a distance z_0 from the radiating aperture is evaluated as the flux of the real part of the Poynting vector through the surface of a cylinder of height z_0 and radius $\rho_{\mathrm{NN}}/\lambda_0 = j_{0,1} \csc \theta_0 / 2\pi$ [the surface integral is limited to the region containing the central maximum of $J_0(k_\rho \rho)$, because we are not interested in the power transported by the tails] where ρ_{NN} is the radial distance of the first null of the J_0 Bessel funtion. This calculation is repeated for different distances z_0 from the aperture and different beam waist parameters $\tilde{w}_0$ for a radiating aperture with $\rho_{\mathrm{ap}} = 25\lambda_0$ and $\theta_0 \simeq 25°$ and reported in Fig. 5, where the power flux has been normalized to the initial power
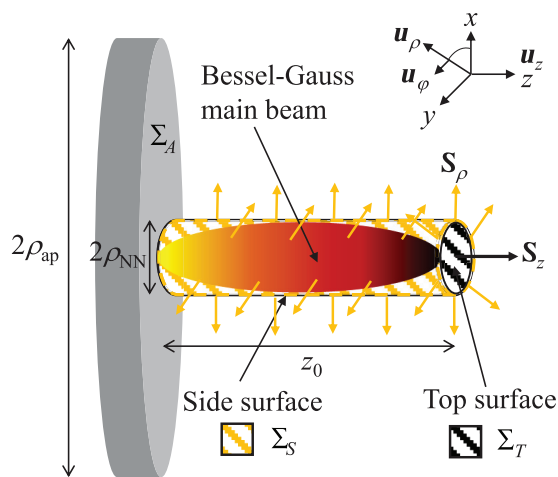
flowing through the entire radiating aperture (and not to the input power inside the cylinder). Consequently, the normalized power flux through the total cylinder surface is always less than 1, and gives a measure of the abovementioned power-transport efficiency. The contribution given by the vertical S_z and radial S_ρ components of the Poynting vector are shown separately and then summed to give a complete picture.

As expected from theory, for $\tilde{w}_0 \to 0$, BGBs show power transport features similar to GBs: the power flux transported along the axis of propagation is efficiently confined, but only for a few wavelengths. On the other hand, for $\tilde{w}_0 > \tilde{w}_{0,\mathrm{lim}}$, the power flux transported along the axis of propagation is more uniformly distributed along z_0, never reaching the efficiency of a GB, but remaining stable for several wavelengths, up to the nondiffractive range. In this regard, it is worth stressing here that the results of Fig. 5 further corroborate the importance of $z_{\mathrm{ndr}}^{\mathrm{BG}}$ [as given by Eq. (8)], which is marked with a white continuous line and accurately predicts the maximum distance at which a BGB is expected to efficiently transport power along the propagation axis; beyond that point, the power mainly flows along the radial direction, i.e., transverse to the axis of propagation. For the sake of completeness, the limit set by the asymptotic nondiffractive range z_{ndr} is marked with a white dashed line and is reached by $z_{\mathrm{ndr}}^{\mathrm{BG}}$ for $\tilde{w}_0 > \tilde{w}_{0,\mathrm{lim}}$. As a final remark, we note that Fig. 5 suggests using a beam waist parameter in the range $0.4 < \tilde{w}_0 < 0.6$; in this range, the power transport efficiency attains satisfactory values and is evenly distributed along $\bar{z}_0$. We should stress that this specific range partially depends on the initial choice of $\rho_{\mathrm{ap}} = 25\lambda_0$ and $\theta_0 = 25°$. However, a different choice of these parameters would not change the results from a qualitative viewpoint, the only differences being an axis scale on z_0 and a scale factor of the power flux, both due to the change of the nondiffractive range.

IV. LEAKY-WAVE SYNTHESIS PROCEDURE FOR BESSEL-GAUSS BEAMS

In this section we illustrate the synthesis of a BGB considering a leaky-wave structure operating in the microwave range, i.e., a radially periodic array of microstrip rings printed on a grounded dielectric slab and centered on the vertical z axis (see Fig. 6 and the related Table I). Such a reference "bull-eye" (BE) configuration is excited by a VED source placed along the z axis on the ground plane; by symmetry, this radiates an azimuthally invariant TM^z field.

A. Synthesis procedure

The BE design is based on a modal analysis of its linearized version (see, e.g., Ref. [35] and the references therein), namely a linear array of straight microstrip lines, which has a discrete translational symmetry and hence
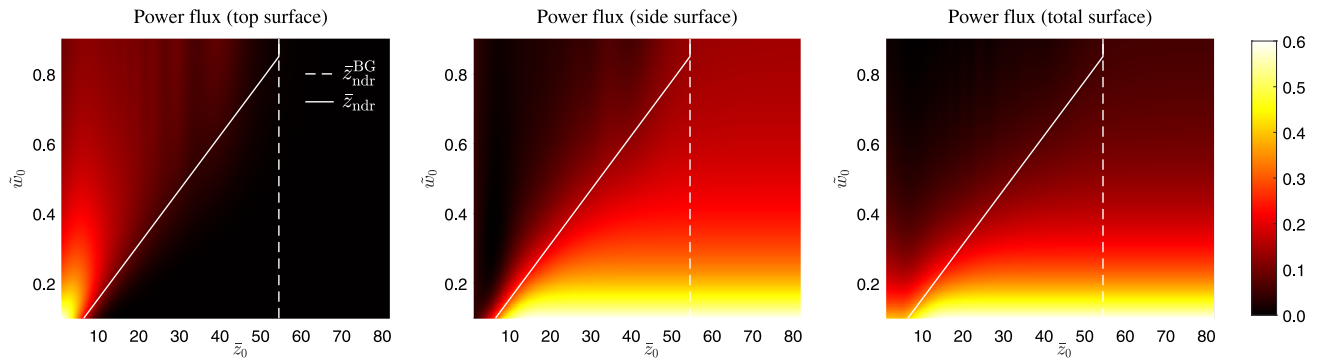

FIG. 4. A schematic representation of the power flux carried out by the main beam of a BGB generated by a radiating aperture.

FIG. 5.   From left to right, the power flux over the top surface $\int_{\Sigma_T} d\sigma\, S_z$, the power flux over the side surface $\int_{\Sigma_S} d\sigma\, S_\rho$, and the power flux over the whole surface ($\int_{\Sigma_T} d\sigma\, S_z + \int_{\Sigma_S} d\sigma\, S_\rho$) (each normalized to the power through the entire radiating aperture $\int_{\Sigma_A} d\sigma\, S_z$) are shown as a function of $\bar{z}_0 = z_0/\lambda_0$ and $\tilde{w}_0$. The white continuous and dashed lines represent the limits set by $\bar{z}_{\mathrm{ndr}}^{\mathrm{BG}}$ and $\bar{z}_{\mathrm{ndr}}$, respectively.

supports Bloch modes customarily representable in terms of space harmonics via Floquet theorem. By operating within a frequency range where the dominant TM leaky Bloch mode radiates through a *single* radiative space harmonic in a *backward* regime, the desired inward BE aperture distribution can be synthesized, as shown in [35] where the same structure was used to generate LW BBs.

In this case, however, the strict radial periodicity of the bull-eye must be relaxed, in order to obtain a Gaussian radial decay in amplitude of the aperture field. This can be achieved by means of a *radial tapering* procedure, i.e.,
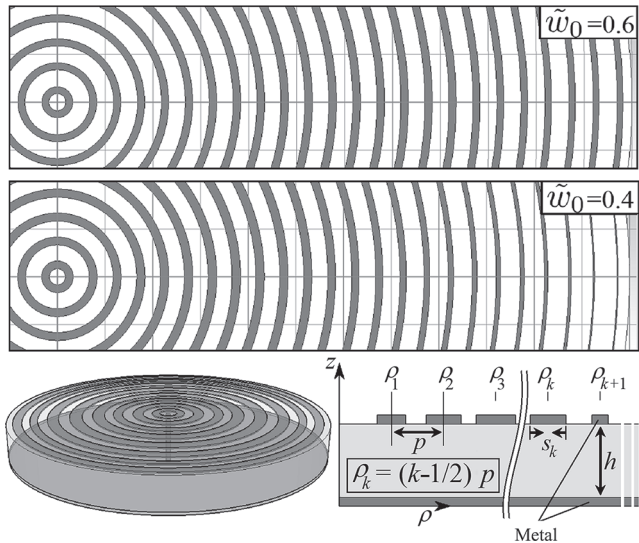

FIG. 6.   The planar leaky-wave structure designed here to radiate a BGB: a radially periodic ("bull-eye") arrangement of microstrip rings printed on a grounded dielectric substrate and excited by a VED source. The top and middle rows show the simulated structures associated to $\tilde{w}_0 = 0.6$ and $\tilde{w}_0 = 0.4$, respectively, while the lower inset shows a schematic representation of the structure: a perspective view on the left and a radial section on the right. The values of the relevant geometrical parameters are listed in Table I.

by gradually varying the geometry of the annular array in the radial direction, in order to modulate the value of the leaky-mode attenuation constant and thus to synthesize the desired amplitude distribution of the aperture field E_z (see, e.g., Ref. [37]). In particular, the geometrical parameter varied to achieve such a modulation in the reference BE structure considered here is the width s of the annular metal strips (the other, unchanged, physical parameters being the radial period $p = 0.6\lambda_0 = 10$ mm, the substrate thickness $h = 0.188\lambda_0 = 3.14$ mm, and the substrate relative permittivity $\varepsilon_r = 2.2$, assuming the operating frequency $f = 18$ GHz).

In Fig. 7(a), the normalized phase and attenuation constants of the radiative space harmonic of the TM leaky mode supported by the linearized BE are reported as a function of the ratio s/p at the fixed frequency $f = 18$ GHz. Let us focus first on $\hat{\alpha}_\rho$: this starts from 0 at $s/p = 0$ (corresponding to a bare grounded slab with no microstrip, which supports a bound TM surface wave), then raises to a single maximum $\hat{\alpha}_\rho^{\mathrm{max}} \simeq 0.04$, attained approximately at $s/p = 0.55$, and then monotonically decreases again to 0 at $s/p = 1$ (corresponding to a closed parallel-plate waveguide, which supports a bound TEM mode).

Turning now to $\hat{\beta}_\rho$, it can be observed that a very mild variation occurs when s/p varies between 0 and 0.55,

TABLE I.   Design parameters.

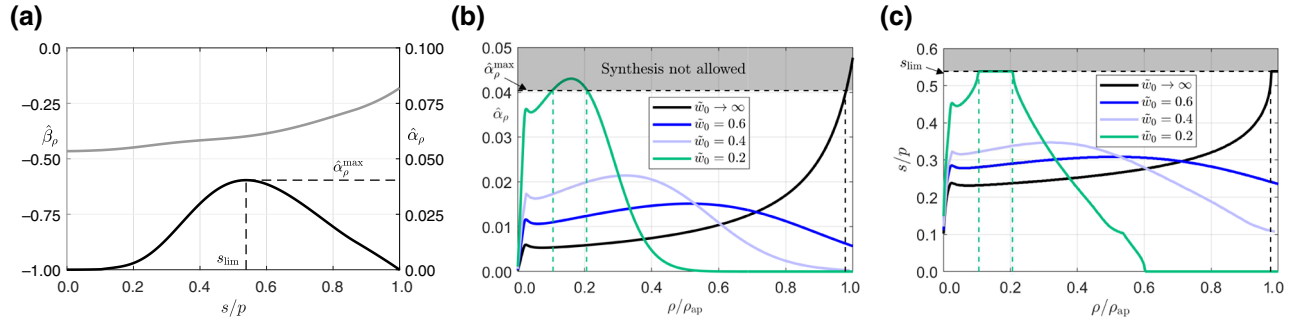| Parameter	$\tilde{w}_0 = 0.6$ Value (mm)	$\tilde{w}_0 = 0.4$ Value (mm)
h	3.14	3.14
ρ_{ap}	234	234
$s_1, \ldots, s_4$	2.86, 2.84, 2.87, 2.92	3.25, 3.25, 3.33, 3.40
$s_5, \ldots, s_8$	2.96, 3.00, 3.04, 3.07	3.47, 3.52, 3.55, 3.55
$s_9, \ldots, s_{12}$	3.10, 3.12, 3.13, 3.14	3.53, 3.46, 3.35, 3.21
$s_{13}, \ldots, s_{16}$	3.14, 3.14, 3.11, 3.06	3.04, 2.86, 2.67, 2.46
$s_{17}, \ldots, s_{20}$	3.01, 2.94, 2.86, 2.76	2.26, 2.06, 1.85, 1.63
$s_{21}, \ldots, s_{24}$	2.67, 2.56, 2.44, 2.40	1.41, 1.22, 1.10, 1.07

FIG. 7. (a) Normalized phase and attenuation constants of the radiative space harmonic of the fundamental TM leaky mode supported at $f = 18$ GHz by a linearized BE structure as in Fig. 6 with radial period $p = 10$ mm, substrate thickness $h = 3.14$ mm, and substrate relative permittivity $\varepsilon_r = 2.2$, as a function of the ratio between the strip width s and p. (b) Radial profiles of the normalized attenuation function required for synthesizing a BGB aperture field as in Eq. (13), for different values of the normalized beam waist $\tilde{w}_0$. (c) Radial profiles of the ratio s/p corresponding to the cases shown in (b).

with an average value $\hat{\beta}_\rho \simeq -0.4$ corresponding to the axicon angle $\theta_0 \simeq 26°$, and a maximum angular variation $\Delta\theta_0 < \pm 2°$ from the average value θ_0. This is a very desirable condition, since it ensures that the effect of the radial BE tapering on the axicon angle is negligible, i.e., the rays emitted at different radii are nearly parallel and hence a transverse Bessel structure of the near field can be synthesized, as discussed in Sec. II.

The radial profile of $\hat{\alpha}_\rho$ required to synthesize a desired aperture distribution $E_\rho^{ap}(\rho)$ can be obtained from the following formula, originally derived in Ref. [39]:

$$\hat{\alpha}_\rho(\rho) = \frac{\lambda_0}{4\pi}$$
$$\times \frac{\rho|E_\rho^{ap}(\rho)|^2}{(1/\eta)\int_{\rho_0}^{\rho_{ap}}\rho'|E_\rho^{ap}(\rho')|^2 d\rho' - \int_{\rho_0}^{\rho}\rho'|E_\rho^{ap}(\rho')|^2 d\rho'}. \quad (12)$$

Here ρ_0 is the minimum radius of the radiating aperture and η is the radiation efficiency (the ratio between the radiated power and the input power).

We should stress here that the synthesis procedure can be applied to either the vertical or the radial component of the electric field, leading to the same results. For the vertical component, the aperture distribution of a BGB is given in Eq. (6). For the radial component [according to Eqs. (6) and (10)], the aperture field distribution reads

$$E_\rho^{ap}(\rho) = H_1^{(2)}(\beta_\rho\rho)e^{-(1/2)(\rho/w_0)^2}. \quad (13)$$

Here we used the synthesis procedure on the radial component because it allows for a more straightforward calculation of the near-field distribution through Eq. (11).

In Fig. 7(b) radial profiles of $\hat{\alpha}_\rho$ are reported, obtained from Eqs. (12) and (13) with $\rho_0 = \lambda_0/100 \simeq 0.166$ mm, $\rho_{ap} = 14\lambda_0 \simeq 234$ mm, and $\eta = 0.9$ for different values of the normalized BGB waist parameter $\tilde{w}_0 = 0.2, 0.4, 0.6$, and $+\infty$ (the latter corresponding to a pure BB). It can be

noted that all these profiles are synthesizable, i.e., they lie below the upper limit $\hat{\alpha}_\rho^{max} \simeq 0.04$, except for small portions (highlighted with vertical dashed colored lines) of those for $\tilde{w}_0 = 0.2$ and $+\infty$.

The corresponding radial profiles of s/p are reported in Fig. 7(c) (where the ranges corresponding to values of $\hat{\alpha}_\rho > \hat{\alpha}_\rho^{max}$ have been trimmed to $s_{lim}/p \simeq 0.55$). The selected values for the radial period $p = 10$ mm and the aperture radius $\rho_{ap} = 234$ mm correspond to having a number $N = 24$ of microstrip rings. Once the radial profile of s/p has been obtained, it can be discretized to define the width of each microstrip ring and thus complete the BE design.

B. Results

In order to validate the effectiveness of this design procedure, full-wave electromagnetic simulations have been performed using the software package CST Microwave Studio. In Figs. 8(a)–8(f) colormaps for the absolute value of E_z are reported along an arbitrary azimuthal plane, obtained by considering different aperture fields relevant to the designs for $\tilde{w}_0 = 0.6$ and 0.4.

In particular, in Figs. 8(a) and 8(d) we show the field radiated by the ideal aperture distribution (13), whereas in Figs. 8(b) and 8(e) we show the field radiated by the aperture distribution reconstructed from the radial profiles of the attenuation constant obtained from Eq. (12). Specifically, Figs. 8(b) and 8(e) are obtained by assuming an aperture field given by

$$E_\rho^{ap} = \sqrt{\frac{2\pi\alpha_\rho(\rho)}{\rho}}\exp\left[-2\int_{\rho_0}^{\rho_{ap}}\alpha_\rho(\rho')d\rho'\right]e^{j\angle H_1^{(2)}(\beta_\rho\rho)}, \quad (14)$$

with $\alpha_\rho(\rho')$ given by Eq. (12). According to the leaky-wave tapering techniques reported in Refs. [37,39],
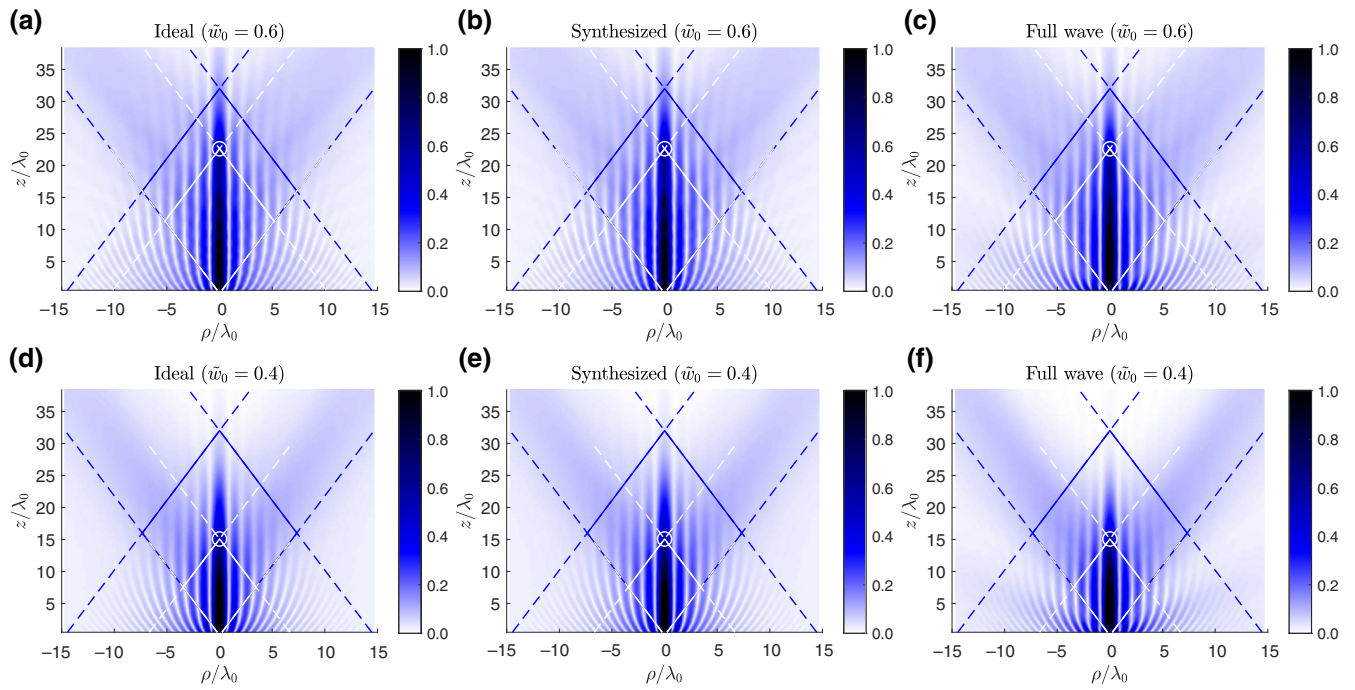
FIG. 8.   Colormaps showing the absolute value of E_z in an arbitrary azimuthal ρ-z plane for BGBs having two different values of the normalized waist: $\tilde{w}_0 = 0.4$ and 0.6. (a),(d) fields radiated by the ideal aperture distribution (13); (b),(e) fields radiated by the aperture distribution synthesized through the radial tapering of the attenuation constant via Eq. (12); (c),(f) full-wave results obtained with CST for the actual BE structure designed as described in Sec. IV A. The blue dashed lines represent the shadow boundaries expected for a BB (i.e., $\tilde{w}_0 \to \infty$), whereas the white dashed lines represent the shadow boundaries expected for a BGB as predicted by Eq. (8). White circles mark the numerical evaluations of $z_{\mathrm{ndr}}^{\mathrm{BG}}$ (note the close agreement with the intersection point of the shadow boundaries).

Eq. (14) with Eq. (12) accurately reconstruct the aperture field in Eq. (13). Indeed, the two sets of insets [i.e., Figs. 8(a), 8(b) and Figs. 8(d), 8(e)] are virtually identical, thus validating the effectiveness of the aperture-field synthesis.

In Figs. 8(c) and 8(f) we report instead the field obtained through full-wave simulations performed with CST. A comparison with the other insets shows that the near field produced by the designed structures perfectly reproduces

those of the corresponding ideal BGBs. This comparison fully validates the proposed synthesis procedure.

In Figs. 9(a)–9(b), radial profiles of E_z are reported, evaluated at $z = z_{\mathrm{ndr}}^{\mathrm{BG}}$ and $z = z_{\mathrm{ndr}}^{\mathrm{BG}}/2$, again for the two designs with $\tilde{w}_0 = 0.6$ [see Fig. 9(a)] and $\tilde{w}_0 = 0.4$ [see Fig. 9(b)]. In particular, the full-wave results (continuous lines) are compared with the ideal profiles given by $J_0(k_\rho \rho)$ and $J_0(k_\rho \rho)e^{-\rho^2/(2w_0^2)}$. Good agreement can be observed over the beam maximum and over the first two
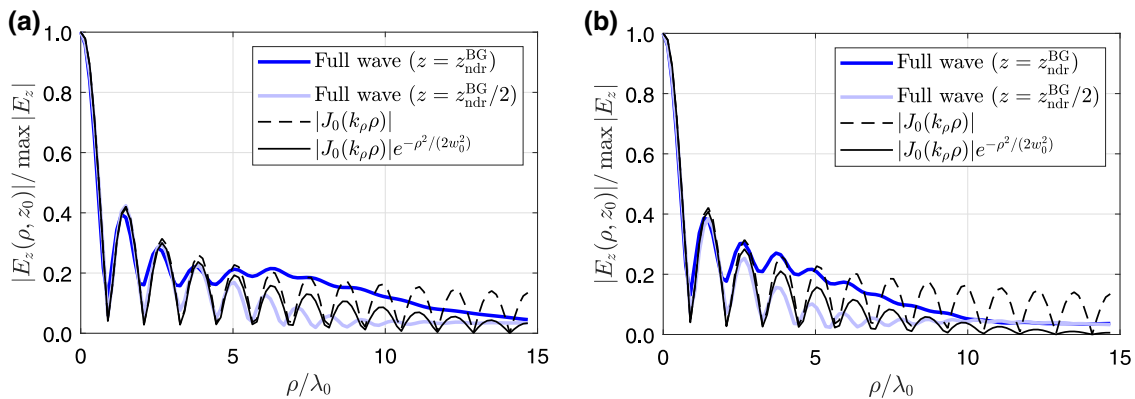

FIG. 9.   Transverse radial profiles of $|E_z|$ evaluated at $z = z_{\mathrm{ndr}}^{\mathrm{BG}}$ and $z = z_{\mathrm{ndr}}^{\mathrm{BG}}/2$ for (a) $\tilde{w}_0 = 0.6$ and (b) $\tilde{w}_0 = 0.4$: comparison between full-wave results obtained by simulating in CST an actual BE structure and ideal Bessel and Bessel-Gauss profiles.

side lobes. More generally, one can observe in the simulations the expected decrease of the side-lobe level of the near-field distribution, which is a direct consequence of the Gaussian tapering of the aperture field.

V. DISCUSSION AND CONCLUSION

In this work we investigate the diffractive and focusing properties of Bessel-Gauss beams accounting for the vectorial nature of the electromagnetic fields and without resorting to the paraxial approximation. As opposed to well-established scalar techniques considered in optics, the proposed vectorial, nonparaxial approach allows for discussing the generation of Bessel-Gauss beams at microwave frequencies. Here, the microwave generation of Bessel-Gauss beams has been obtained through leaky waves, and corroborated with accurate full-wave simulations of two different leaky-wave structures exhibiting remarkable diffractive and focusing properties in agreement with the initial theoretical predictions.

Indeed, we start our analysis recalling and comparing the diffractive and focusing properties of *classical* Bessel beams, *leaky-wave* Bessel beams (i.e., Bessel beams generated through leaky waves), and Bessel-Gauss beams. A ray interpretation of the radiation mechanism provide simple closed-form expressions for predicting the Bessel-Gauss beam nondiffractive properties. These formulae have been validated relying on both numerical procedures and full-wave simulations showing a remarkable accuracy. Moreover, the numerical results provide the rationale for using Bessel-Gauss beams in place of their asymptotic counterparts, i.e., Bessel beams and Gaussian beams. In fact, Bessel-Gauss beams offer two degrees of freedom, the initial beam waist parameter and the axicon angle, to counterbalance their focusing and nondiffractive character: a trade-off that either Bessel or Gaussian beams can handle with only one degree of freedom (the axicon angle for the former, the initial beam waist for the latter).

In particular, a numerical analysis of the power flux transported over a given area at different distances from the aperture reveals that a proper selection of the initial beam waist for a given axicon angle allows for obtaining a Bessel-Gauss beam whose radiative properties may be extremely attractive in modern focusing applications. These results provide the design criteria for the choice of the initial beam waist parameter.

On this basis, leaky-wave theory has been proposed to synthesize the needed aperture field and the corresponding leaky-wave structure. Specifically, a radially periodic leaky-wave antenna consisting of a grounded dielectric slab covered with periodic annular metallic strips has been considered. Resorting to leaky-wave tapering procedures, we find that, by properly modulating the width of the metallic strips, it is possible to generate Bessel-Gauss beams with initial beam-waist parameter within the range identified in the previous analysis. Two different structures have been designed accordingly and validated through accurate full-wave simulations.

These results are expected to be of great significance in modern microwave applications, such as wireless near-field links, where the focusing character, the cover distance, and the power-transport efficiency always represent a concern.

APPENDIX: EVALUATION OF THE NONDIFFRACTIVE RANGE FOR BESSEL-GAUSS BEAMS

The definition of $z_{\mathrm{ndr}}^{\mathrm{BG}}$ (see Sec. II) requires the correct evaluation of the vertical distance at which the amplitude of the field halves its initial value. However, the singular behavior of the aperture field at $\rho = 0$, $z = 0$ (see the comments in Sec. III A) hinders the correct estimation of the nondiffractive range according to its definition. In Fig. 10 we outline the procedure carried out to correctly estimate $z_{\mathrm{ndr}}^{\mathrm{BG}}$. First, the points p_1 (blue triangle) and p_2 (blue reverse triangle) representing the first local minimum after the initial sharp peak and the last local maximum before the final vanishing tail, respectively, are found. Second, a linear regression between p_1 and p_2 is used to project the point y_0 (blue square) onto the $z = 0$ axis, which represents the *virtual* initial amplitude of the field. This value is halved, $y_0/2$ (green square), and projected back onto the curve at p_0 (see green diamond) through the linear map to finally get an estimation of $z_{\mathrm{ndr}}^{\mathrm{BG}}$ (green circle).
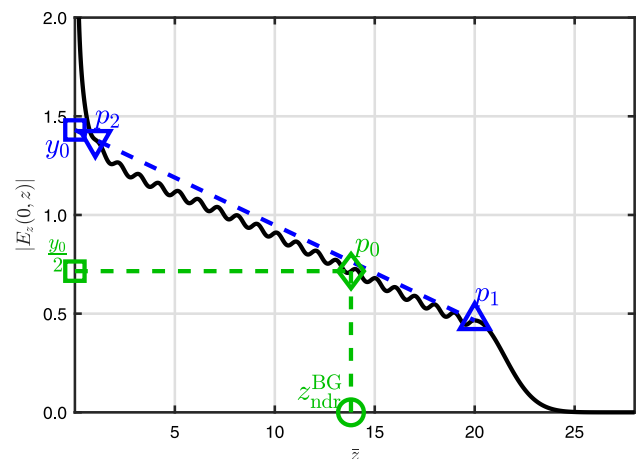

FIG. 10. Schematic representation of a typical field-amplitude decay $|E(0,z)|$ along the z axis for a BGB. The numerical procedure employed for the calculation of $z_{\mathrm{ndr}}^{\mathrm{BG}}$ is schematically reported in the figure and explained in detail in the text.

[1] J. A. Stratton, *Electromagnetic Theory* (John Wiley & Sons, Hoboken, NJ, USA, 1941).

[2] J. Durnin, Exact solutions for nondiffracting beams. I. The scalar theory, J. Opt. Soc. Am. A **4**, 651 (1987).

[3] J. Durnin, J. J. Miceli, Jr., and J. H. Eberly, Diffraction-Free Beams, Phys. Rev. Lett. **58**, 1499 (1987).

[4] J. Durnin, J. H. Eberly, and J. J. Miceli, Jr., Comparison of Bessel and Gaussian beams, Opt. Lett. **13**, 79 (1988).

[5] M. Anguiano-Morales, A. Martínez, M. D. Iturbe-Castillo, S. Chávez-Cerda, and N. Alcalá-Ochoa, Self-healing property of a caustic optical beam, Appl. Opt. **46**, 8284 (2007).

[6] C. Palma, G. Cincotti, G. Guattari, and M. Santarsiero, Imaging of generalized Bessel–Gauss beams, J. Mod. Opt. **43**, 2269 (1996).

[7] F. Gori, G. Guattari, and C. Padovani, Bessel–Gauss beams, Opt. Commun. **64**, 491 (1987).

[8] P. L. Greene and D. G. Hall, Properties and diffraction of vector Bessel–Gauss beams, J. Opt. Soc. Am. A **15**, 3020 (1998).

[9] S. Ruschin, Modified Bessel nondiffracting beams, J. Opt. Soc. Am. A **11**, 3224 (1994).

[10] R. M. Herman and T. Wiggins, Apodization of diffractionless beams, Appl. Opt. **31**, 5913 (1992).

[11] A. Cox and J. D'Anna, Constant-axial-intensity nondiffracting beam, Opt. Lett. **17**, 232 (1992).

[12] S. Y. Popov and A. T. Friberg, Apodization of generalized axicons to produce uniform axial line images, Pure Appl. Opt. **7**, 537 (1998).

[13] P. Vahimaa, V. Kettunen, M. Kuittinen, J. Turunen, and A. T. Friberg, Electromagnetic analysis of nonparaxial Bessel beams generated by diffractive axicons, J. Opt. Soc. Am. A **14**, 1817 (1997).

[14] J. Turunen, A. Vasara, and A. T. Friberg, Holographic generation of diffraction-free beams, Appl. Opt. **27**, 3959 (1988).

[15] S. N. Khonina and I. Golub, Optimization of focusing of linearly polarized light, Opt. Lett. **36**, 352 (2011).

[16] R. Borghi, M. Santarsiero, and F. Gori, Axial intensity of apertured bessel beams, J. Opt. Soc. Am. A **14**, 23 (1997).

[17] M. Martınez-Corral, G. Saavedra, P. Andres, and F. Gori, Analytical formulation of the axial behavior of apodized general Bessel beams, Opt. Commun. **169**, 1 (1999).

[18] Z. Hricha, L. Dalil-Essakali, and A. Belafhal, Axial intensity distribution and focal shifts of focused partially coherent conical bessel–gauss beams, Opt. Quant. Electron. **35**, 101 (2003).

[19] D. Ding and X. Liu, Approximate description for Bessel, Bessel–Gauss, and Gaussian beams with finite aperture, J. Opt. Soc. Am. A **16**, 1286 (1999).

[20] V. Bagini, F. Frezza, M. Santarsiero, G. Schettini, and G. Schirripa Spagnolo, Generalized Bessel–Gauss beams, J. Mod. Opt. **43**, 1155 (1996).

[21] B. Lü and W. Huang, Three-dimensional intensity distribution of focused Bessel–Gauss beams, J. Mod. Opt. **43**, 509 (1996).

[22] R. Borghi, M. Santarsiero, and M. A. Porras, Nonparaxial Bessel–Gauss beams, J. Opt. Soc. Am. A **18**, 1618 (2001).

[23] P. L. Overfelt and C. S. Kenney, Comparison of the propagation characteristics of Bessel, Bessel–Gauss, and Gaussian beams diffracted by a circular aperture, J. Opt. Soc. Am. A **8**, 732 (1991).

[24] Z. Bouchal and M. Olivík, Non-diffractive vector Bessel beams, J. Mod. Opt. **42**, 1555 (1995).

[25] Z. Bouchal, Nondiffracting optical beams: Physical properties, experiments, and applications, Czech. J. Phys. **53**, 537 (2003).

[26] M. Ettorre and A. Grbic, Generation of propagating Bessel beams using leaky-wave modes, IEEE Trans. Antennas Propag. **60**, 3605 (2012).

[27] W. Fuscaldo, G. Valerio, A. Galli, R. Sauleau, A. Grbic, and M. Ettorre, Higher-order leaky-mode Bessel-beam launcher, IEEE Trans. Antennas Propag. **64**, 904 (2016).

[28] M. Ettorre, S. C. Pavone, M. Casaletti, M. Albani, A. Mazzinghi, and A. Freni, in *Aperture Antennas for Millimeter and Sub-Millimeter Wave Applications*, edited by A. Boriskin and R. Sauleau (Springer, Cham, Switzerland, 2018), p. 243.

[29] M. A. Salem, A. H. Kamel, and E. Niver, Microwave Bessel beams generation using guided modes, IEEE Trans. Antennas Propag. **59**, 2241 (2011).

[30] S. C. Pavone, M. Ettorre, M. Casaletti, and M. Albani, Transverse circular-polarized Bessel beam generation by inward cylindrical aperture distribution, Opt. Express **24**, 11103 (2016).

[31] M. Albani, A. Mazzinghi, and A. Freni, Automatic design of CP-RLSA antennas, IEEE Trans. Antennas Propag. **60**, 5538 (2012).

[32] M. Ettorre, M. Casaletti, G. Valerio, R. Sauleau, L. Le Coq, S. C. Pavone, and M. Albani, On the near-field shaping and focusing capability of a radial line slot array, IEEE Trans. Antennas Propag. **62**, 1991 (2014).

[33] B. G. Cai, Y. B. Li, W. X. Jiang, Q. Cheng, and T. J. Cui, Generation of spatial Bessel beams using holographic metasurface, Opt. Express **23**, 7593 (2015).

[34] P. Lemaitre-Auger, S. Abielmona, and C. Caloz, Generation of Bessel beams by two-dimensional antenna arrays using sub-sampled distributions, IEEE Trans. Antennas Propag. **61**, 1838 (2013).

[35] D. Comite, W. Fuscaldo, S. K. Podilchak, P. D. H. Re, V. Gómez-Guillamón Buendía, P. Burghignoli, P. Baccarelli, and A. Galli, Radially periodic leaky-wave antenna for Bessel beam generation over a wide-frequency range, IEEE Trans. Antennas Propag. **66**, 2828 (2018).

[36] W. Fuscaldo, D. Comite, A. Boesso, P. Baccarelli, P. Burghignoli, and A. Galli, Focusing Leaky Waves: A Class of Electromagnetic Localized Waves with Complex Spectra, Phys. Rev. Appl. **9**, 054005 (2018).

[37] A. A. Oliner, in *Antenna Engineering Handbook*, edited by R. C. Johnson (McGraw-Hill, New York, NY, USA, 1984), Chap. 10.

[38] J. L. Gómez-Tornero, F. Quesada-Pereira, A. Alvarez-Melcon, G. Goussetis, A. R. Weily, and Y. J. Guo, Frequency steerable two dimensional focusing using rectilinear leaky-wave lenses, IEEE Trans. Antennas Propag. **59**, 407 (2010).

[39] J. L. Gómez-Tornero, D. Blanco, E. Rajo-Iglesias, and N. Llombart, Holographic surface leaky-wave lenses with circularly-polarized focused near-fields–Part I: Concept,

design and analysis theory, IEEE Trans. Antennas Propag. 61, 3475 (2013).

[40] D. Blanco, J. L. Gómez-Tornero, E. Rajo-Iglesias, and N. Llombart, Holographic surface leaky-wave lenses with circularly-polarized focused near-fields–Part II: Experiments and description of frequency steering of focal length, IEEE Trans. Antennas Propag. 61, 3486 (2013).

[41] S. Chávez-Cerda, A new approach to Bessel beams, J. Mod. Opt. 46, 923 (1999).

[42] M. Albani, S. C. Pavone, M. Casaletti, and M. Ettorre, Generation of non-diffractive Bessel beams by inward cylindrical traveling wave aperture distributions, Opt. Express 22, 18354 (2014).

[43] L. Felsen, Real spectra, complex spectra, compact spectra, J. Opt. Soc. Am. A 3, 486 (1986).

[44] S. C. Pavone, M. Ettorre, and M. Albani, Analysis and design of Bessel beam launchers: Longitudinal polarization, IEEE Trans. Antennas Propag. 64, 2311 (2016).

[45] A. Ip and D. R. Jackson, Radiation from cylindrical leaky waves, IEEE Trans. Antennas Propag. 38, 482 (1990).

[46] P. Burghignoli, W. Fuscaldo, D. Comite, P. Baccarelli, and A. Galli, Higher-order cylindrical leaky waves–Part I: Canonical sources and radiation formulas, IEEE Trans. Antennas Propag. 67, 6735 (2019).

[47] M. Abramowitz and I. A. Stegun, *Handbook of Mathematical Functions* (Dover, New York, NY, USA, 1962).

[48] T. Tamir and A. A. Oliner, Guided complex waves. Part 1: Fields at an interface, Proc. IEE 110, 310 (1963).

[49] T. Tamir and A. A. Oliner, Guided complex waves. Part 2: Relation to radiation patterns, Proc. IEE 110, 325 (1963).

[50] W. Fuscaldo and S. C. Pavone, Metrics for localized beams and pulses, IEEE Trans. Antennas Propag. 68, 1176 (2020).